ADVANCED MATERIALS INTERFACES
www.advmatinterfaces.de

Improve Hole Collection by Interfacial Chemical Redox Reaction at a Mesoscopic NiO/$CH_3NH_3PbI_3$ Heterojunction for Efficient Photovoltaic Cells

Ming-Wei Lin, Kuo-Chin Wang, Jeng-Han Wang, Ming-Hsien Li, Yu-Ling Lai, Takuji Ohigashi, Nobuhiro Kosugi, Peter Chen, Der-Hsin Wei, Tzung-Fang Guo, and Yao-Jane Hsu**

Organometal-trihalide-perovskite-based solar cells have exhibited high efficiencies when incorporated into mesoscopic NiO (NiO_{nc}) hole-transport layers. The integration of a NiO_{nc}-perovskite heterojunction provides an inorganic alternative as a p-type contact material with efficient hole extraction for perovskite-based solar cells. Herein the origin of such highly efficient carrier transport is studied in terms of electronic, chemical and transport properties of a NiO_{nc}-perovskite heterojunction with X-ray photoelectron spectra, ultraviolet photoelectron spectra, near-edge X-ray absorption fine structure spectra, a scanning transmission X-ray microscope, and calculations of electronic structure. A pronounced chemical redox reaction is found at an NiO_{nc}-perovskite heterojunction such that PbI_2 is oxidized to PbO with subsequent formation of hole-dopant $CH_3NH_3PbI_{3-2\delta}O_\delta$ at the heterojunction. The generation of hole-doping $CH_3NH_3PbI_{3-2\delta}O_\delta$ induced by the redox reaction at the NiO_{nc}/perovskite heterojunction plays a significant role to facilitate the carrier transport, and thus enhances the photovoltaic efficiencies.

1. Introduction

Solution-processable organic photovoltaic cells with merits of mass production, versatile functionality, and low production costs play an important role in conventional thin-film technologies. The aim for power conversion efficiency (PCE) comparable with that of an organic solar cell is generally limited by the energetic loss involved in separating or transferring the bound charges from the absorber following photoexcitation. A way to overcome this limitation is to employ solution-processable thin-film absorbers, in which the photoinduced electrons and holes can separate with minimal cost of energy. As an emerging solution-processable material, an organic–inorganic perovskite hybridized compound ($CH_3NH_3PbI_3$, also denoted as $MAPbI_3$) attracts intensive attention for optoelectronic applications.[1–9] Early work focused on utilizing small $MAPbI_3$ nanoparticles to sensitize TiO_2 with an iodide liquid electrolyte, and produced a PCE below 7% because of the instability of the perovskite in a highly polar liquid electrolyte.[2,3] A remarkable advance for perovskite solar cells (PSC) was obtained on replacing the liquid hole-transporting medium with a solid-state organic hole-transport material (HTM) composed of 2,2′,7,7′-tetrakis-(*N*,*N*-di-*p*-methoxyphenylamine)-9,9′-bifluorene (spiro-OMeTAD).[6] Through controlling the formation of the perovskite layer and the contact electrode materials, PSC at the state of the art have a remarkably improved PCE over 19%.[10,11] PSC employing inorganic HTM (i.e., nickel oxide (NiO), copper iodine (CuI), copper(I) thiocyanate (CuSCN), and graphene oxide) currently attract much attention because of their greater mobility, effective transparency in the visible region, and satisfactory chemical stability.[12–16] Among these inorganic HTM, NiO is promising to be a cathode interlayer candidate for PSC because of its wide bandgap and electronic properties, such as control of Ni:O stoichiometry and appropriate alignment of the band-edge position with that of perovskite. The first report of PSC based on a metal-oxide p-type semiconductor of nickel-oxide (NiO_x) as hole-transport layer delivered PCE = 7.8% using a structure similar to that of organic photovoltaics.[17] Since then, PSC employing NiO as a p-type contact have been widely investigated, with remarkable progress in photovoltaic performance. A comprehensive review summarizes the recent progress of NiO p-type-contact-based PSC in detail.[15] A perovskite device at the state of the

Dr. M.-W. Lin, Y.-L. Lai, Dr. D.-H. Wei, Dr. Y.-J. Hsu
National Synchrotron Radiation Research Center
Hsinchu 30076, Taiwan, Republic of China
E-mail: yjhsu@nsrrc.org.tw
Dr. K.-C. Wang, Dr. M.-H. Li,
Dr. P. Chen, Prof. T.-F. Guo
Department of Photonics
National Cheng Kung University
Tainan 70101, Taiwan, Republic of China
E-mail: petercyc@mail.ncku.edu.tw
Dr. J.-H. Wang
Department of Chemistry
National Taiwan Normal University
Taipei 10610, Taiwan, Republic of China
Dr. T. Ohigashi, Prof. N. Kosugi
UVSOR Synchrotron
Institute for Molecular Science
Myodaiji, Okazaki 444-8585, Japan
Dr. P. Chen, Prof. T.-F. Guo, Dr. Y.-J. Hsu
Research Center for Energy Technology and Strategy (RCETS)
National Cheng Kung University
Tainan 70101, Taiwan, Republic of China

DOI: 10.1002/admi.201600135

art using pulsed-laser deposition of a high-quality nanostructured p-type NiO electrode achieved PCE = 17.3% which is near the best inverted *p*-i-*n* PSC (18.1%) using PEDOT:PSS.[18,19] These results demonstrate the promising potential of replacing organic HTM or a hole extraction layer with inorganic NiO.

Since that hole extraction is highly dependent on offsets of energy levels at the perovskite/HTM interfaces.[20–25] NiO exhibits an appropriate alignment of the valence-band (VB) edge with that of perovskite, which is favorable for efficient hole extraction as demonstrated from the photoluminescence (PL) and transient absorption spectra,[13,14,26] but these reported energy levels −5.2 eV (VB of NiO) and −5.4 eV (VB of perovskite) are generally measured with pristine materials. The real chemical environment at the real NiO/perovskite heterojunction remains unknown. The aim of our present work is to scrutinize the interfacial chemical properties with various surface-sensitive spectral techniques and calculations of electronic structure. We found that a chemical redox reaction occurred at the NiO/perovskite heterojunction, which might modify the energy levels at the interface and contribute some impact on the photovoltaic performance.

2. Results and Discussion

The related current–voltage (*I*–*V*) characteristics of photovoltaic devices made of mesoscopic NiO_{nc}/perovskite/$PC_{61}BM$ heterojunction solar cell have been published in our previous work.[13] The best-performing cell using $PC_{61}BM$ delivered high V_{oc} of 1040 mV with short-circuit photocurrent density (J_{sc}) of 13.24 mA cm^{-2} and 69% fill factor, leading to an overall PCE of 9.51%. Herein we focus on the origin of such highly efficient carrier transport in terms of electronic, chemical, and transport properties of a NiO_{nc}-perovskite heterojunction. We applied deposition in two steps to prepare the $MAPbI_3$ perovskite. In this process, PbI_2 dissolved in *N*,*N*-dimethylformamide was spin-coated onto a NiO_{nc} substrate; the substrate was then dipped into a CH_3NH_3I (MAI) solution that was dissolved in 2-propanol to produce $MAPbI_3$. **Figure 1**a shows the depth profile of a survey X-ray photoelectron spectra (XPS) for ITO/NiO_{nc}/$MAPbI_3$ etched with sputtered Ar ions. In the figure, a blue line, representing ITO/NiO_{nc}/$MAPbI_3$ before etching, displays several evident signals for carbon 1s (C 1s) and nitrogen 1s (N 1s), lead 4f (Pb 4f), and iodine 3d (I 3d) that reveal characteristic signals of perovskite $MAPbI_3$. The oxygen (O) and nickel (Ni) that are features of NiO_{nc} were not observed because of the surface sensitivity of XPS. For the surface sputtered with Ar ions for 90 min, the red spectrum displays clear evident Ni 2p, O 1s, Pb 4f, and I 3d features. The broad emission located at 250 eV is assigned as Ar $2p_{1/2}$ and Ar $2p_{3/2}$. Besides, the peak located at around 320 eV is assigned as Ar 2s. These signals are arising from Ar sputter. As the atomic sensitivity factors[27,28] of C 1s and N 1s are a tenth those of Pb 4f and I 3d, the intensities of C 1s and N 1s are small in the $MAPbI_3$ and greatly decreased after ion sputtering. To examine the distribution of composition near the interface between perovskite and bottom NiO_{nc}, we estimated the stoichiometry of perovskite at the top and at the NiO_{nc}/$MAPbI_3$ interface with an intensity ratio of Pb 4f and I 3d, described by

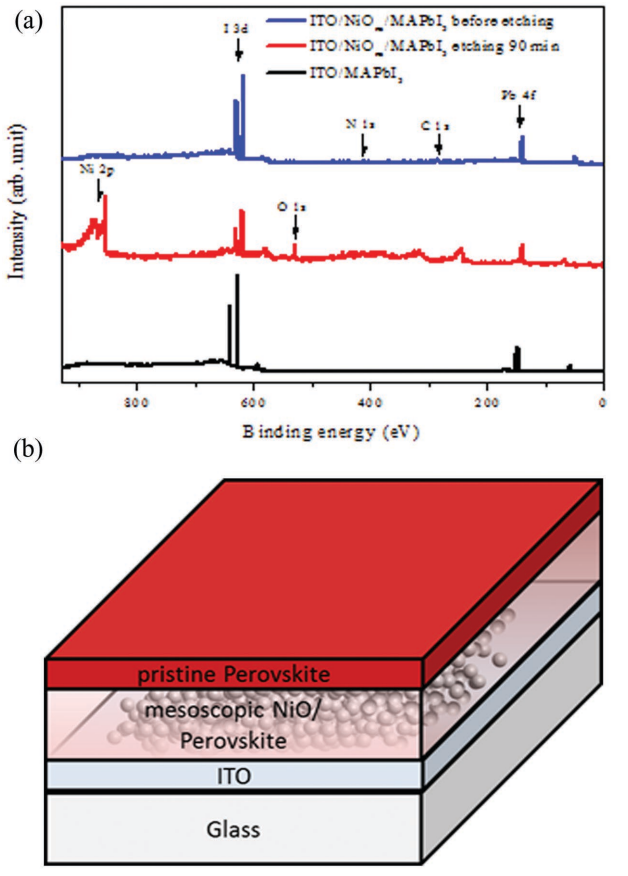

Figure 1. a) XPS depth profile of survey spectra for an ITO/NiO_{nc}/$MAPbI_3$ perovskite sample etched with sputtered Ar ions. The blue line represents before etching, and red line is the surface sputtered by Ar ions for 90 min. The ITO/$MAPbI_3$ in the black line is fabricated for comparison. The incident synchrotron photon energy is 1100 eV. b) Schematic of the ITO/NiO_{nc}/$MAPbI_3$ structure. The scheme illustrates a gradient structure of a NiO_{nc}/$MAPbI_3$ perovskite layer. Pristine $MAPbI_3$ is on top followed by an interface layer near the NiO_{nc}-$MAPbI_3$ perovskite heterojunction.

$$\left(\frac{I_{I\ 3d}/ASF_{I\ 3d}}{I_{Pb\ 4f}/ASF_{Pb\ 4f}}\right) \quad (1)$$

We found that the value varied from the top perovskite layer (≈4) to near the interface layer (≈3), which implies that a composition gradient exists in the perovskite film, especially at the interface region. Compared with ITO/$MAPbI_3$ (black line in Figure 1a), the spectrum demonstrates a value ≈4, which differs from sputtered samples. The results indicate that NiO_{nc} is involved in an interfacial reaction at the heterojunction. On the whole, the analysis of the depth profile of the NiO_{nc}/$MAPbI_3$ perovskite layer discloses that the composition is not homogeneous as expected, but exhibits a distribution dependent on depth, especially near the NiO_{nc}-perovskite interface. Figure 1b is a schematic illustration of a varied structure of a NiO_{nc}/$MAPbI_3$ perovskite layer; the pristine $MAPbI_3$ is at the top, followed by an interface layer near the NiO_{nc}-$MAPbI_3$ perovskite heterojunction.

To clarify the composition of the interface layer, we inspected the chemical states and electronic structures of the perovskite layer with synchrotron XPS and near-edge X-ray absorption

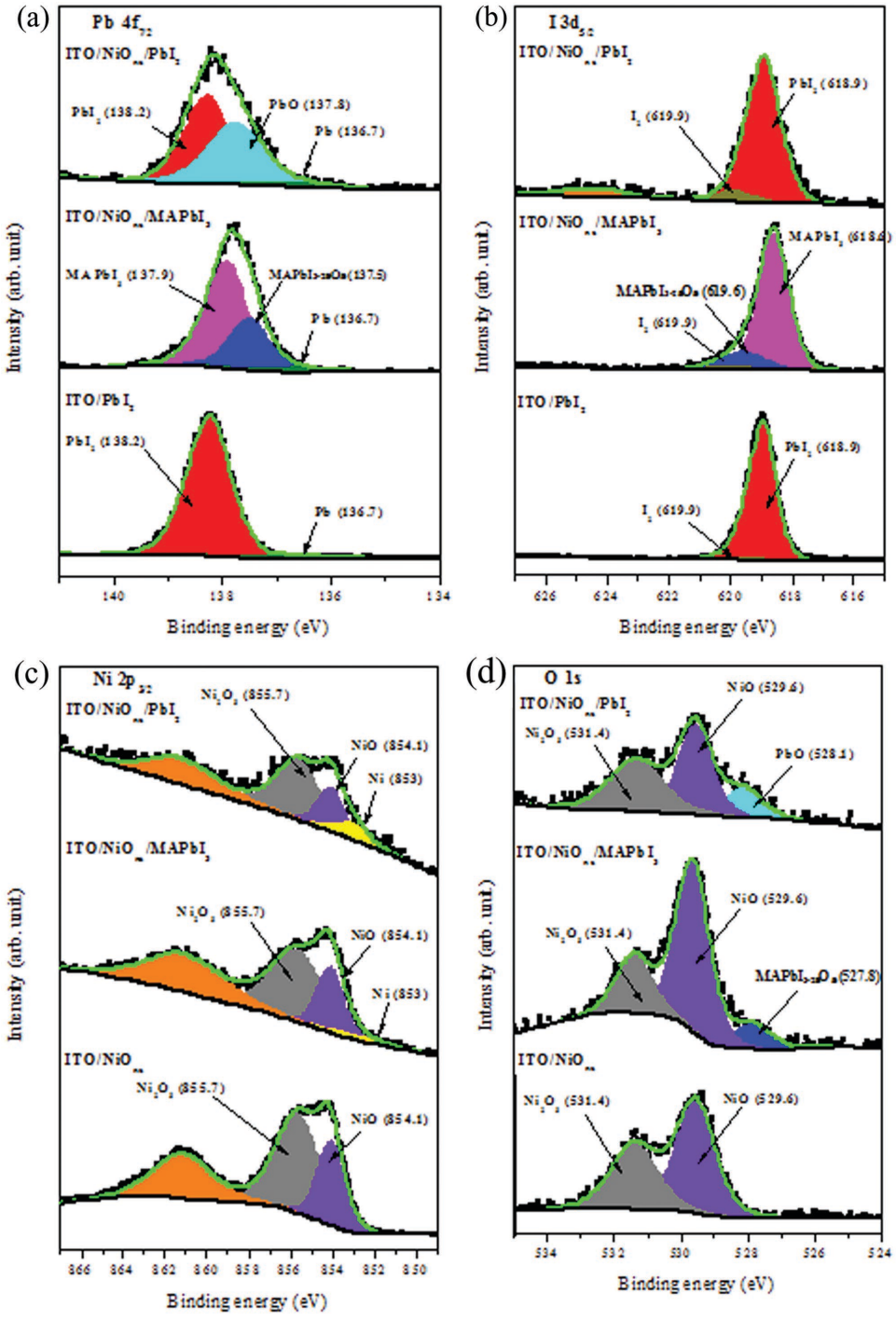

Figure 2. XPS of a) Pb $4f_{7/2}$, b) I $3d_{5/2}$, c) Ni $2p_{3/2}$, and d) O 1s of ITO/NiO_{nc}/PbI_2, ITO/NiO_{nc}/$MAPbI_3$, with ITO/NiO_{nc} and ITO/PbI_2 samples for comparison.

fine structure (NEXAFS) spectra. XPS of Pb $4f_{7/2}$ for ITO/NiO_{nc}/PbI_2 and ITO/NiO_{nc}/$MAPbI_3$ are shown in **Figure 2**a. The Pb $4f_{7/2}$ spectrum displays binding energy (BE) 138.2 eV for ITO/NiO_{nc}/PbI_2 (as seen in Figure 2a-top), but smaller BE 137.9 eV for ITO/NiO_{nc}/$MAPbI_3$ (as seen in Figure 2a-middle). These Pb XPS results show a negative BE shift 0.3 eV when ITO/NiO_{nc}/PbI_2 further reacted with the MAI solution.[29] The spin-orbit splitting between Pb $4f_{7/2}$ and Pb $4f_{5/2}$ is 4.9 eV for all cases (Pb $4f_{5/2}$ not shown herein), which agrees satisfactorily with the literature.[29–31] On spectral deconvolution, the ITO/NiO_{nc}/PbI_2 sample exhibits three features at BE 138.2, 137.8, and 136.7 eV, which are attributed separately to PbI_2, PbO,[32] and Pb. The Pb $4f_{7/2}$ spectrum of ITO/NiO_{nc}/$MAPbI_3$ is composed of three signals at BE 137.9, 137.5, and

136.7 eV, which are assigned to $MAPbI_3$, $MAPbI_{3-2\delta}O_\delta$, and Pb, respectively. Relative to the Pb $4f_{7/2}$ signal of ITO/PbI_2 in Figure 2a-bottom, similar signals of PbI_2 at 138.2 eV and Pb at 136.7 eV are simultaneously detected for ITO/PbI_2 and ITO/NiO_{nc}/PbI_2, but the PbO component is not found for the ITO/PbI_2 sample that has a narrower Pb $4f_{7/2}$ signal. From an analysis of the composition, we found a new feature of $MAPbI_{3-2\delta}O_\delta$ in ITO/NiO_{nc}/$MAPbI_3$ and PbO in ITO/NiO_{nc}/PbI_2.

Figure 2b shows an I $3d_{5/2}$ signal at binding energy 618.9 eV for ITO/NiO_{nc}/PbI_2 and 618.6 eV for ITO/NiO_{nc}/$MAPbI_3$ with spin-orbit splitting 11.5 eV for I $3d_{3/2}$ for all samples.[29,31] With deconvolution, we found that the ITO/NiO_{nc}/PbI_2 spectrum was composed of two clear features at BE 619.9 and 618.9 eV, which are assigned to I_2 and PbI_2, respectively. From the corresponding I $3d_{5/2}$ of reference sample ITO/PbI_2 (in Figure 2b-bottom), we observed a major signal at BE 618.9 eV for PbI_2 and a weak I_2 feature at 619.9 eV. The residual I_2 is more noticeable for ITO/NiO_{nc}/PbI_2 than for ITO/PbI_2, which might be caused by the reduction of NiO to metallic Ni (detailed discussion follows). After the ITO/NiO_{nc}/PbI_2 sample was immersed in MAI solution, the I 3d signal comprised three discernible features at 619.9 eV for I_2, 619.6 eV for $MAPbI_{3-2\delta}O_\delta$, and 618.6 eV for $MAPbI_3$.

Ni $2p_{3/2}$ spectra are shown in Figure 2c. For the ITO/NiO_{nc} sample (Figure 2c-bottom), two features at 854.1 and 855.7 eV are attributed to NiO and Ni_2O_3 states, respectively.[33–35] The peak located at 861 eV is attributed to satellite feature.[36] After deposition of PbI_2 on NiO_{nc} (Figure 2c-top), an additional feature appearing at smaller binding energy, 853.0 eV, is assigned to metallic Ni.[33–35] On the ITO/NiO_{nc}/$MAPbI_3$ surface (Figure 2c-middle), not much variation after MAI deposition on the ITO/NiO_{nc}/PbI_2 surface was observed, except a decreased intensity of metallic Ni at 853.0 eV. This result indicates that the signal of metallic Ni at 853.0 eV originated from reduction of NiO interacting with PbI_2. The metallic Ni may effectively decrease the contact resistance of anode/active layer interface, which is favorable for hole extraction from active layer to the anode.[37] On the other hand, from the thermal dynamic point of view, we cannot exclude the formation of NiI_2 as NiO reacted with PbI_2, because the peaks of Ni 2p and I 3d for NiI_2 are almost overlapped with Ni 2p of Ni_2O_3 and I 3d of PbI_2 in XPS. As a result, the metallic Ni or NiI_2 was formed at the interface.

Corresponding O 1s spectra appear in Figure 2d. The features of Ni_2O_3, NiO, and PbO are clearly seen at 531.4, 529.6, and 528.1 eV after PbI_2 deposition on NiO_{nc}; shown in Figure 2d-top, the former two signals are at the same position with ITO/NiO_{nc} (Figure 2d-bottom). As a result, the formation of metallic nickel and PbO indicates an interfacial redox reaction when NiO_{nc} was processed with PbI_2. Through pouring an MAI solution on ITO/NiO_{nc}/PbI_2 to form the perovskite, PbO became involved to form $MAPbI_{3-2\delta}O_\delta$ at 527.8 eV. In consequence, the XPS indicate that a chemical redox reaction occurred at the heterojunction of NiO_{nc}/$MAPbI_3$. To explore in further detail beneath the NiO_{nc}, we recorded NEXAFS spectra with Auger electron yield (AEY) and total electron yield measurements (TEY). Because NEXAFS directly probes the unoccupied electronic states, it is powerful to examine the redox species from the interface near the NiO_{nc} substrate.

Figure 3a,b shows NEXAFS spectra of the Ni L_3-edge for ITO/NiO_{nc}, ITO/NiO_{nc}/PbI_2, and ITO/NiO_{nc}/$MAPbI_3$ in TEY and Auger electron spectra (AES) modes, respectively. Both TEY spectra and AES are indicated to show a gradual shift toward smaller photon energy for the Ni L_3-edge of ITO/NiO_{nc}/PbI_2 (red line) and ITO/NiO_{nc}/$MAPbI_3$ (blue line) relative to ITO/NiO_{nc} (green line). The smaller energy shift for ITO/NiO_{nc}/PbI_2 originated mainly from Ni reduction at the NiO_{nc}/PbI_2 heterojunction. On inspection of ITO/NiO_{nc}/$MAPbI_3$ (processed with MAI), the spectrum is similar to that of ITO/NiO_{nc}/PbI_2 because the Ni reduction occurred at the NiO_{nc}/PbI_2 interface. The spectral line width is noticeably smaller for the AES than the TEY mode because AES probes the surface near the interface, but TEY detects simultaneously both surface and bulk information of NiO_{nc}.

The corresponding O *K*-edge NEXAFS spectra of ITO/NiO_{nc}, ITO/NiO_{nc}/PbI_2, and ITO/NiO_{nc}/$MAPbI_3$ in TEY spectra and AES are recorded in Figure 3c and 3d, separately. The TEY spectrum of ITO/NiO_{nc} (green line in Figure 3c) exhibits three major features at 532.1, 537.4, and 540.4 eV, which are assigned to band transitions mainly from O 1s to Ni 3d-O 2p hybridized orbitals for the first line and Ni 4s4p-O 2p for the other two lines. This result indicates that the spectrum of pristine NiO agrees satisfactorily with previous data.[38–44] The O *K*-edge TEY spectra of ITO/NiO_{nc}/PbI_2 (red line) and ITO/NiO_{nc}/$MAPbI_3$ (blue line) are similar to those of ITO/NiO_{nc} (green line). As a result, the O *K*-edge in the TEY mode illustrates that the variation caused by the redox reaction at the heterojunction of PbI_2 and $MAPbI_3$ on NiO_{nc} is limited. In contrast, the AEY spectra shown in Figure 3d demonstrate an additional distinct feature at 534.5 eV for ITO/NiO_{nc}/PbI_2, and at 535.1 eV for ITO/NiO_{nc}/$MAPbI_3$ (also seen in the inset), beyond three major signals specified above, O 1s to Ni 3d-O 2p at 532.1 eV and to Ni 4s4p-O 2p at 537.4 and 540.4 eV. These additional features are apparently produced by the contact reaction at the heterojunction of NiO_{nc}/PbI_2 and NiO_{nc}/$MAPbI_3$. The intensity of the signal at 532.1 eV gradually decreased, but the other features about 535–545 eV became broader because of a new shoulder feature emerging at a greater photon energy for NiO_{nc}/PbI_2 and NiO_{nc}/$MAPbI_3$.

For the ITO/NiO_{nc} sample, the feature at 532.1 eV is a transition of the O 1s electron to unoccupied Ni 3d-O 2p hybridized states that has a main character of Ni 3d. The shape and intensity of the feature hence depend on the Ni site symmetry, the occupation number of the d levels and the O—Ni bond length.[45–47] Upon deposition of PbI_2, the decreased intensity of the feature at 532.1 eV reveals unambiguously that the $3d^8(Ni^{2+}) - 2p^6(O^{2-})$ mixing is weakened through the interfacial redox reaction. The reduction of Ni^{2+} to Ni^0 leads to a decreased number of 3d vacancies of nickel, and hence results in a decreased hybridization of O 2p states with the Ni 3d states.[48]

The other signals of pure NiO_{nc} about 535–545 eV are transitions to O 2p containing a mixed character of O 2p, Ni 4s, and 4p states.[46] Similarly, upon PbI_2 deposition, the variation of the number of 4s and 4p vacancies also leads to a change of $4s4p(Ni^{2+}) - 2p(O^{2-})$ mixing, and hence to a variation of the signal intensities. As a result, the interfacial redox reaction diminishes the Ni site symmetry and distorts the local structure around the O or Ni atom, resulting in an increased degree of disorder in the NiO_{nc} system, and hence altering the intensities and shapes of the scattering resonances at 537.4 and 540.4 eV.

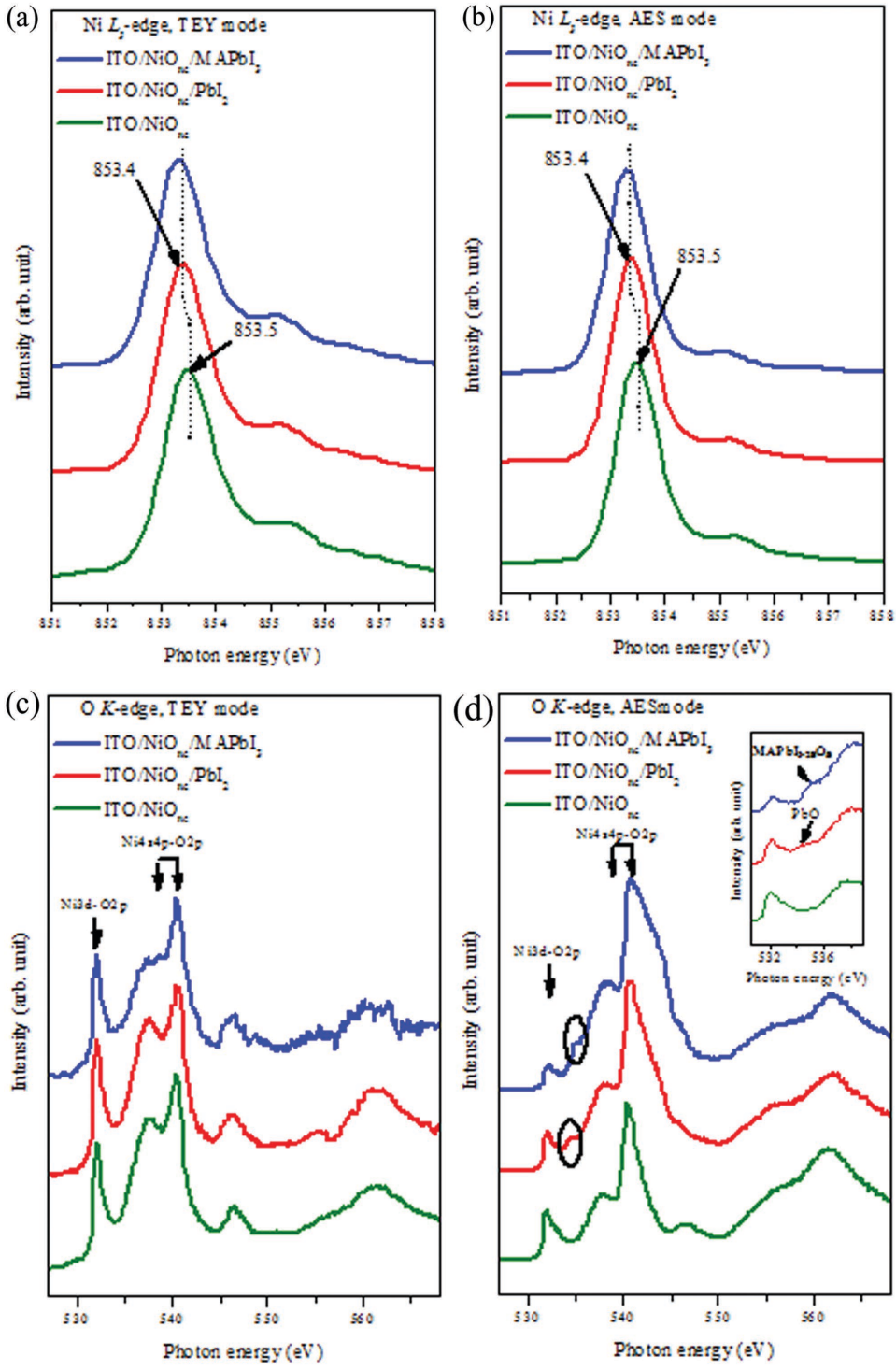

Figure 3. NEXAFS spectra of the Ni L_3-edge in a) TEY and b) AES modes, and O K-edge spectra in c) TEY and d) AES modes for ITO/NiO$_{nc}$, ITO/NiO$_{nc}$/PbI$_2$, and ITO/NiO$_{nc}$/MAPbI$_3$. The green line represents ITO/NiO$_{nc}$, the red line ITO/NiO$_{nc}$/PbI$_2$, and the blue line ITO/NiO$_{nc}$/MAPbI$_3$.

Mesoporous NiO is effectively used as an anode material to grow $CH_3NH_3PbI_3$ perovskite for a highly efficient organic solar cell. The redox reaction of PbI_2 with a mesoporous NiO electrode determined by XPS, NEXAFS spectra in AES and TEY modes can be described as follows.

$$NiO + PbI_2 \rightarrow PbO + Ni + I_2 \text{ or } PbO + NiI_2 \quad (2)$$

$$PbI_2 + CH_3NH_3I \rightarrow CH_3NH_3PbI_3 \quad (3)$$

$$PbO + CH_3NH_3I \rightarrow CH_3NH_3PbI_{3-2\delta}O_\delta (MAPbI_{3-2\delta}O_\delta) \quad (4)$$

As shown in Equation (2), an interfacial redox reaction occurs between PbI_2 and NiO_{nc}; PbI_2 and NiO_{nc} reacted to form PbO when PbI_2 was spin-coated on NiO_{nc}. In addition to the formation of perovskite from PbI_2 and CH_3NH_3I, the consequent PbO reacts with CH_3NH_3I to produce oxygen-substituted perovskite, $MAPbI_{3-2\delta}O_\delta$. It is worth noting that the formation of PbO, $MAPbI_{3-2\delta}O_\delta$, I_2, and Ni is clearly observed in XPS and AEY spectra as mentioned above (shown in Figures 2 and 3). The oxygen in $CH_3NH_3PbI_3$ perovskite thus leads to a doping effect, hence influencing the transport of charge carriers to the mesoporous NiO electrode. In the literature, some authors predicted that the defects induced on substitution of Pb or I in $CH_3NH_3PbI_3$ might produce new intraband states in the bandgap to attract an electron or hole.[49–51] Based on their theoretical work, Yan and co-workers proposed that interfaces between the perovskite absorbers and some contact oxides might form a new state to transfer an electron or hole, so to affect the device performance. Although speculation explained the improved large PCE, experimental evidence regarding interfacial states is still unproved. Our results strongly and clearly demonstrate that interfacial reactions induce iodine substitution by O in the formation of perovskite. We expect that

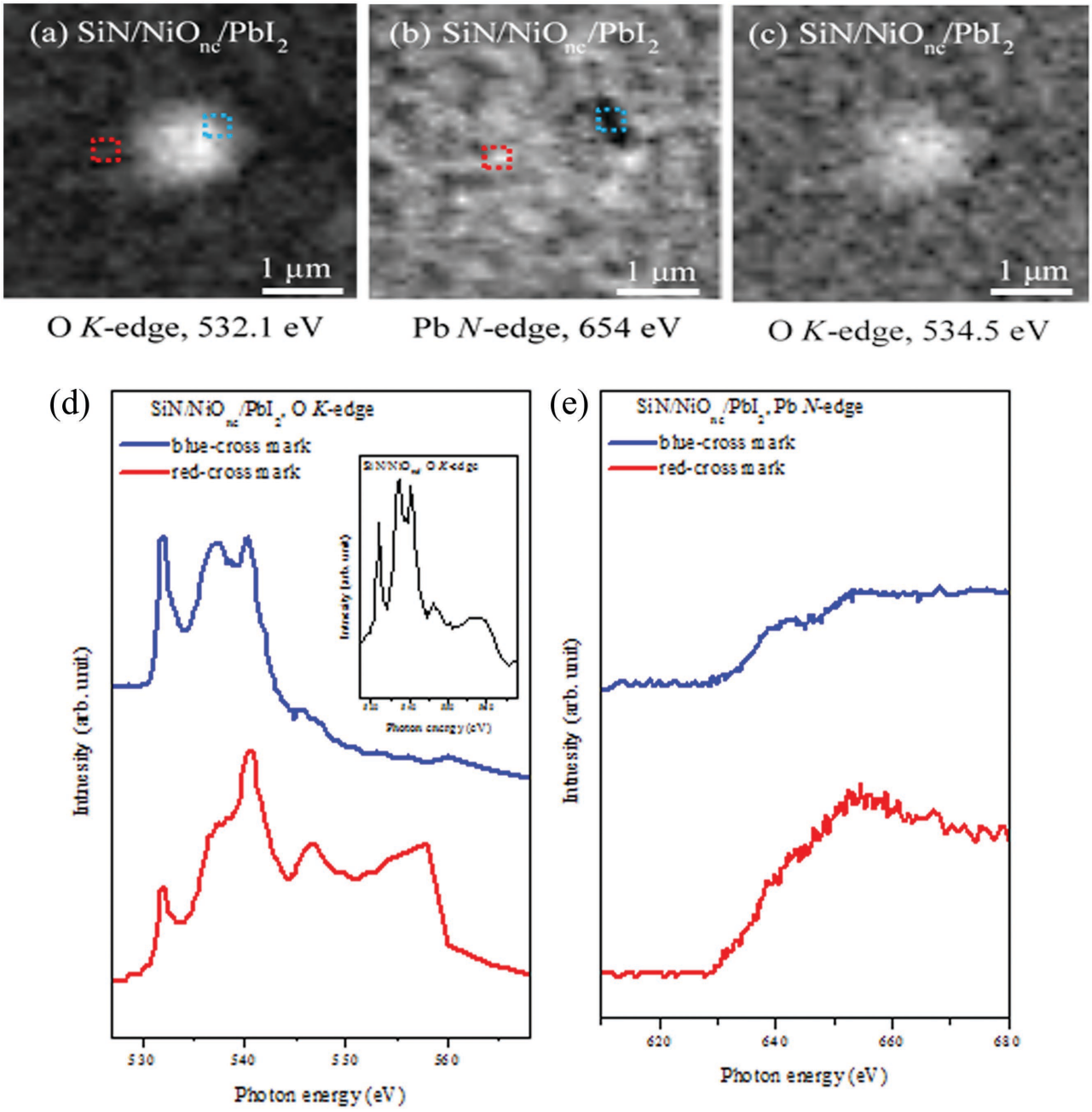

Figure 4. OD images of a) O *K*-edge at 532.1 eV, b) Pb *N*-edge at 654 eV, and c) O *K*-edge at 534.5 eV for $SiN/NiO_{nc}/PbI_2$. The micro-NEXAFS spectra of d) O *K*-edge and e) Pb *N*-edge are extracted from Figure a and b, respectively. The inset in Figure d shows the O *K*-edge NEXAFS of pristine NiO_{nc}.

the substituent doping effect, like $MAPbI_{3-2\delta}O_{\delta}$, might function as a bridge to influence the charge and thus modify the short-circuit photocurrent (J_{sc}) and large filling factor (FF) of the solar cell.

To examine further the interfacial redox reaction at the NiO_{nc} and $CH_3NH_3PbI_3$ heterojunction, we undertook chemical mapping of elemental distributions within micro-aggregates of $SiN/NiO_{nc}/PbI_2$ and $SiN/NiO_{nc}/MAPbI_3$ with a scanning transmission X-ray microscope (STXM), shown in **Figures 4** and **5**, respectively. Figure 4a shows STXM images of $SiN/NiO_{nc}/PbI_2$ from optical-density (OD) mapping of the characteristic absorption feature of the O *K*-edge at 532.1 eV for NiO_{nc}. The Pb OD map of the $SiN/NiO_{nc}/PbI_2$ as shown in Figure 4b was recorded at 654 eV. The brighter contrast in these two images represents greater O and Pb absorption intensities. The image mappings of O and Pb of $SiN/NiO_{nc}/PbI_2$ show a reverse contrast but a similar distribution in morphology and size. When the photon energy was tuned to 534.5 eV (Figure 4c), which marks the characteristic O signal of PbO observed in the AES spectra as mentioned above, the mapping also showed a distribution of morphology and size similar to that at 532.1 eV except a darker contrast in the central spot and

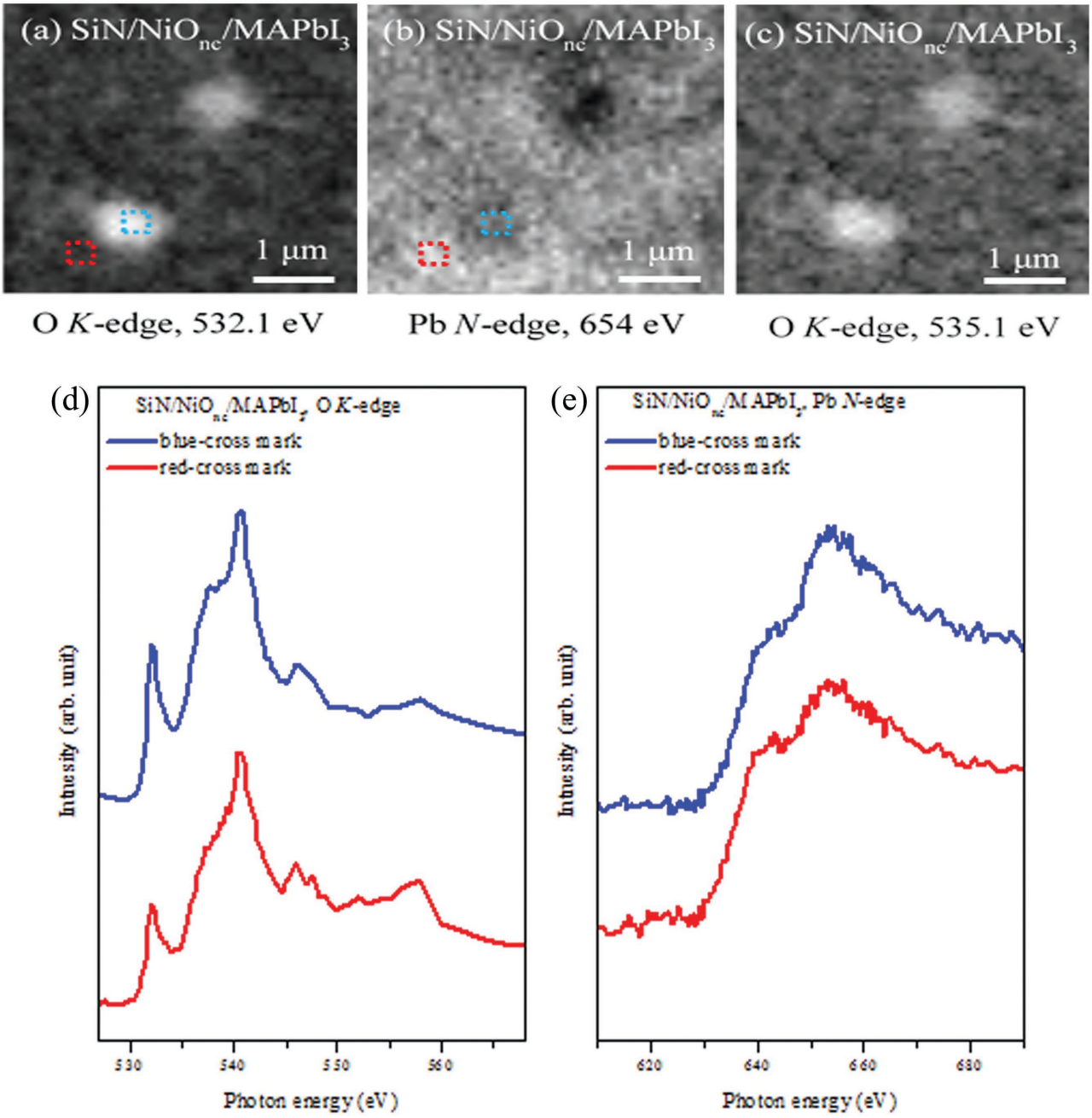

Figure 5. OD images of a) O *K*-edge at 532.1 eV, b) Pb *N*-edge at 654 eV, and c) O *K*-edge at 535.1 eV for $SiN/NiO_{nc}/MAPbI_3$. The micro-NEXAFS spectra of d) O *K*-edge and e) Pb *N*-edge are extracted from Figure a and b, respectively.

a brighter contrast in the vicinity. The brighter central spot is the absorption of a larger cluster in pristine NiO_{nc}, which was used for image tracking during the STXM measurements. The contrast weaker for 532.1 eV but brighter for 534.5 eV in the vicinity indicates that Ni 3d-O 2p mixing is involved in an interfacial redox reaction at the heterojunction and thus decreases the absorption intensity of NiO_{nc} and increases the intensity of associated PbO. As a result, Pb is apparently bonded to O and located on the mesoporous NiO_{nc}.

The micro-NEXAFS spectra extracted from the cross marks depicted in Figure 4a and 4b are shown in Figure 4d and 4e, respectively. The blue- and red-cross marks represent greater and less absorption intensity for O mapping in NiO_{nc} and vice versa for Pb mapping in PbI_2. The NEXAFS spectrum corresponding to pristine NiO_{nc} is shown in the inset of Figure 4d. As mentioned above, the O *K*-edge NEXAFS spectra of $ITO/NiO_{nc}/PbI_2$ exhibit a decreased intensity for the band transition of Ni 3d-O 2p and become broader for the Ni 4s4p-O 2p transition when the interfacial redox reaction occurs. Figure 4d shows the micro NEXAFS spectrum from the blue and red marks in Figure 4a that express a similar variation for the dark area (red mark) but the same curve as pristine NiO_{nc} for the bright area (blue cross). The mark with greater Pb content (red cross in Figure 4b) exhibits a large decreased intensity of the Ni 3d-O 2p transition as shown in Figure 4d. Hence the greater is the extent to which the redox reaction occurs, the less is the intensity of the feature at 532.1 eV, agreeing satisfactorily with the results of the AES NEXAFS spectra.

The O and Pb images of $SiN/NiO_{nc}/MAPbI_3$ that were prepared on soaking the $SiN/NiO_{nc}/PbI_2$ film in MAI solution

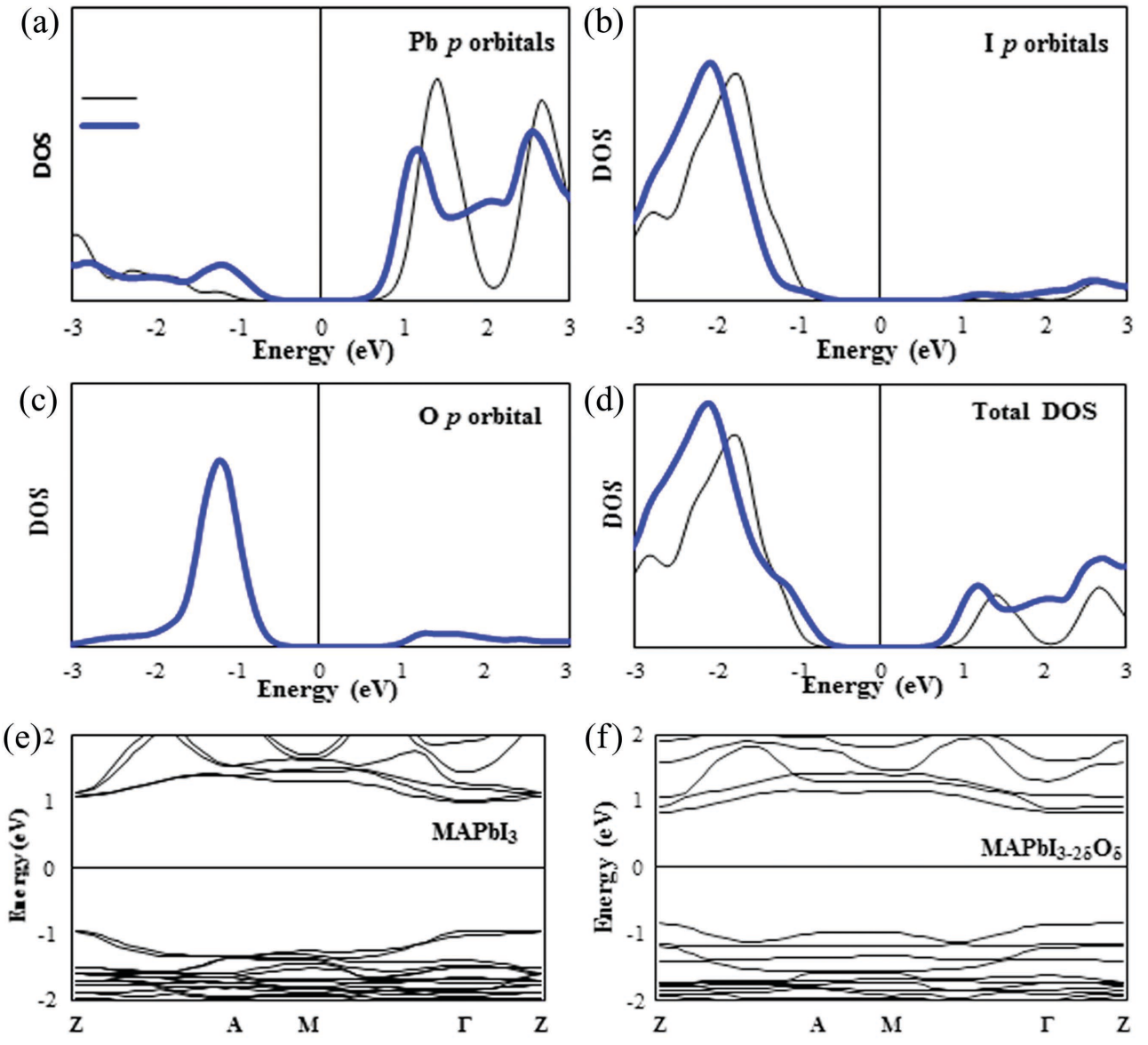

Figure 6. a), b), and c) are Pb, I, and O partial DOS, respectively. d) Total DOS of $MAPbI_3$ and $MAPbI_{3-2\delta}O_\delta$. a–d) The black line represents $MAPbI_3$, the blue line represents $MAPbI_{3-2\delta}O_\delta$. e,f) Calculated band structures for $MAPbI_3$ and $MAPbI_{3-2\delta}O_\delta$. The band edges are 1.94 and 1.67 eV for $MAPbI_3$ and $MAPbI_{3-2\delta}O_\delta$, respectively.

are shown in Figure 5. The O mapping obtained at 532.1 (Figure 5a) and 535.1 eV (Figure 5c), the characteristic signals of NiO_{nc} and $MAPbI_{3-2\delta}O_{\delta}$ observed in AES spectra as mentioned above, displays variations similar to that of SiN/NiO_{nc}/PbI_2. The Pb mapping obtained at 654 eV (Figure 5b) demonstrates a reverse contrast for two large clusters and a brighter dense packing for the others relative to O mapping. All results indicate the growth of perovskite, which is located on the NiO_{nc} mesoporous networks after MAI treatment. The corresponding micro-NEXAFS spectra denoted by cross marks in Figure 5a and 5b are displayed in Figure 5d and 5e for the O *K*-edge and the Pb *N*-edge, respectively. In Figure 5d, both blue and red marks present decreased intensity for the transition Ni 3d-O 2p at 532.1 eV. The small intensity difference of the Ni 3d-O 2p transition of SiN/NiO_{nc}/ $MAPbI_3$ reveals a smaller contribution from pristine NiO_{nc}, which indicates that the redox reaction occurred at the NiO_{nc}-PbI_2 heterojunction. The micro-NEXAFS spectrum of the Pb *N*-edge in Figure 5e also shows a similar shape and intensity. These findings from the microstructures coincide with XPS and NEXAFS spectra.

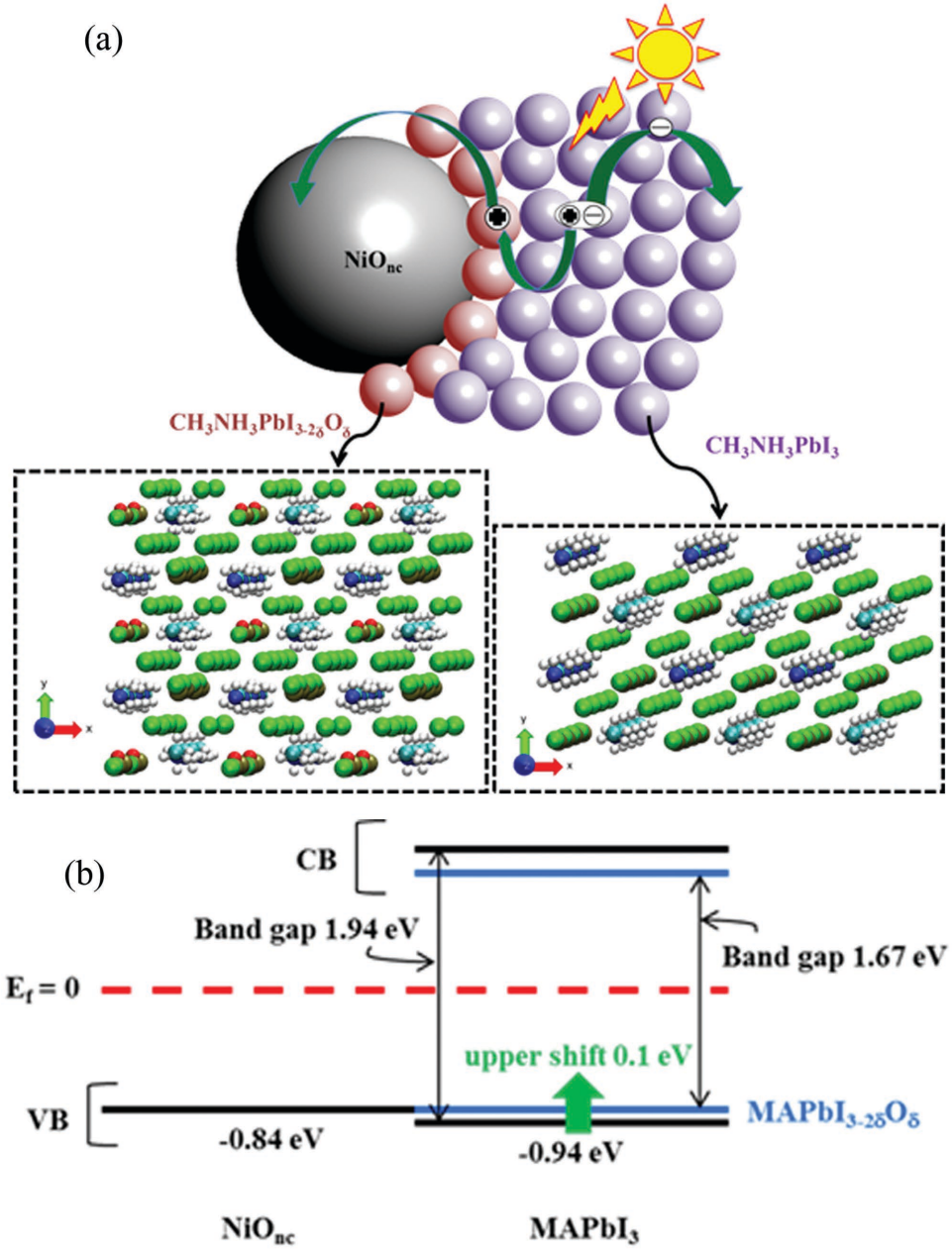

Figure 7. a) Schematic illustration depicting the substitution of two iodine atoms with one O atom. $MAPbI_{3-2\delta}O_{\delta}$ facilitates hole transfer after light extraction from $MAPbI_3$ (Pb: tan balls; I: green balls; N: blue balls; C: cyan balls; H: white balls; O: red balls). b) Band offset of NiO_{nc}: $CH_3NH_3PbI_3$ heterojunction. The upper VB in $CH_3NH_3PbI_{3-2\delta}O_{\delta}$ (upper shift 0.10 eV) indicates a facilitated hole injection from $CH_3NH_3PbI_3$ (–0.94 eV) to NiO_{nc} (–0.84 eV).

Our results indicate that a redox reaction occurred at the NiO_{nc}/PbI_2 heterojunction and formed $MAPbI_{3-2\delta}O_\delta$ in a subsequent reaction.

To explore the role of $MAPbI_{3-2\delta}O_\delta$ in the relation of charge transfer, we calculated the electronic structure (band structure and density of states) based on the perovskite unit cell containing four $MAPbI_3$ units with and without O doping. In perovskite $MAPbI_3$, MA and Pb donate one and two electrons, respectively, to three I ions, forming a band gap 1.94 eV between unoccupied Pb *p* orbital and occupied I *p* orbital (see black lines in **Figure 6**a,b,d,e). MA lacks a significant contribution around the band edge but donates one electron to the Pb-I framework. The minimum of the conduction band (CBM) of $MAPbI_3$ is mainly contributed by the Pb *p* orbital; the valence band edge is mostly occupied by an I *p* orbital as the MA has a limited effect in the band gap, consistent with recent investigation.[52,53] In $MAPbI_{3-2\delta}O_\delta$, on replacing two I with one O, MA and Pb also donate one and two electrons, respectively, but to both I and O that results in a band gap 1.67 eV. The corresponding density of state (DOS) is shown in the blue lines in Figure 6a–d; the band structure is shown in Figure 6f. The value is 13.9% less than that of pristine $MAPbI_3$. In contrast, the VB and CBM are both near the Fermi edge. In consideration of the variation of the VB, the upper VB in $MAPbI_{3-2\delta}O_\delta$ (upper shift 0.10 eV) indicates a facilitated hole injection from $CH_3NH_3PbI_3$ (–0.94 eV) to NiO_{nc} (–0.84 eV). To further confirm the effect of $MAPbI_{3-2\delta}O_\delta$ on facilitating charge transfer, the valence band edges for NiO_{nc}, NiO_{nc}/PbI_2, and $NiO_{nc}/MAPbI_3$ on ITO were determined by ultraviolet photoelectron spectra (UPS) as shown in the Supporting Information. It clearly shows the energy matching of the $NiO_{nc}/MAPbI_3$ interface due to the valence band edge of NiO_{nc}/PbI_2 is shifted toward valence band edge of perovskite. From both aspects on modified NiO_{nc} and interfacial redox, it clearly demonstrates the energy matching facilitates the hole transporting from $MAPbI_3$ to NiO_{nc}.

The redox behavior in a perovskite-mesoporous NiO solar cell is schematically illustrated in **Figure 7**a. The dissolving Pb^{2+} ions from PbI_2 are oxidized to PbO when PbI_2 is in contact with NiO_{nc}. The consequent PbO then reacts with MAI to produce hole-doping $MAPbI_{3-2\delta}O_\delta$, which functions as a gap state between the $MAPbI_3$ and NiO_{nc}. The band offset about the $NiO:CH_3NH_3PbI_3$ heterojunction is drawn in Figure 7b. The reacted $MAPbI_{3-\delta}O_\delta$ makes feasible an opportunity to tune the injection level and thus to influence the hole transport after excitation of $MAPbI_3$. This interfacial hole doping induced by a chemical redox reaction leads to a large J_{sc} and a large FF performance of PSC. Compared to the planar heterojunction of NiO_x/perovskite, the NiO_{nc}/perovskite behaves like a bulk-heterojunction as NiO_{nc} thoroughly contacts with PbI_2 in the process to form $NiO_{nc}/CH_3NH_3PbI_3$ interface due to the large surface area of nanocrystalline. It is anticipated that the effect of $CH_3NH_3PbI_{3-\delta}O_\delta$ on facilitating the hole transport is more apparent in nanocrystalline NiO_{nc}/perovskite than in planar NiO_x/perovskite. In summary, our results indicate that an interfacial optimized hole-transport material for a perovskite solar cell including controlling the perovskite/ hole-transport material is essential for a highly efficient solar cell.

3. Conclusion

In summary, we present the electronic and chemical structures of the heterojunction for $MAPbI_3$ perovskite on mesoporous NiO_{nc}. A depth-profiling study of NiO_{nc}/perovskite indicates that a chemical redox reaction occurred at the heterojunction of NiO_{nc}/PbI_2. We found that PbO forms after PbI_2 is coated on NiO_{nc}, which then reacts with MAI to produce $MAPbI_{3-2\delta}O_\delta$ during the growth of the perovskite. Based on calculations of electronic structure, the formation of $MAPbI_{3-2\delta}O_\delta$ at the $NiO_{nc}/MAPbI_3$ junction is favorable for hole transport from $MAPbI_3$ to NiO_{nc}. This interfacial chemical redox reaction plays a key role in achieving a large J_{sc} and a large FF performance of a PSC that should be taken into consideration in designing highly efficient PSC devices. Our results provide an improved understanding of the interfacial chemical properties of the NiO/perovskite heterojunction. With appropriate surface engineering and control of the energetic profile, we expect highly efficient inverted perovskite solar cells employing NiO to be achievable in the near future.

4. Experimental Section

The mesoporous NiO solution applied to form a mesoscopic layer for spin-coating was made from an NiO slurry and anhydrous ethanol in mass ratio 1:7. The NiO slurry was prepared from NiO nanopowder (Inframat, 3 g) dissolved in ethanol (80 mL), to which was subsequently added ethyl cellulose (15 g, 10 mass% in EtOH) and terpineol (10 g). The solution was stirred, dispersed with an ultrasonic horn and concentrated with a rotary evaporator to remove ethanol to 23 mbar.

CH_3NH_3I was synthesized according to a method described in our previous publication: methylamine (CH_3NH_2) (13.5 mL, 40 mass% in aqueous solution, Alfa Aesar) and hydriodic acid (HI) (15.0 mL, 57 mass% in water, Alfa Aesar) were reacted together in a round-bottomed flask (250 mL) at 0 °C for 2 h with stirring. After the reaction, the solvent was evaporated with a rotary evaporator. Product methyl ammonium iodide (CH_3NH_3I) was formed from the above procedure. The precipitate was washed three times with diethyl ether (Sigma-Aldrich), and dried in a vacuum oven at 60 °C overnight.[5,6,17]

The mesoscopic layer of NiO_{nc} (nc: nanocrystal) was coated on the substrates through spin-coating at 4000 rpm for 30 s. After annealing at 400 °C for 30 min, a p-type mesoporous network was formed, of thickness 250 nm. A sequential deposition method was adopted to fabricate an $NiO_{nc}/MAPbI_3$ layer. Before deposition of PbI_2, the substrates were preheated at 70 °C. PbI_2 solution (1 M in *N*,*N*-dimethylformamide) was spun onto the mesoporous NiO film at 6500 rpm for 90 s, followed by annealing at 70 °C for 30 min. After cooling to room temperature, the resulting films were immersed in 2-propanol to pre-wet the substrates for 5 s, dipped into CH_3NH_3I solution (10 mg mL^{-1} in 2-propanol) for 40 s at room temperature, and annealed at 70 °C for 30 min to complete the perovskite crystallization.

Photoemission spectra and NEXAFS spectra were recorded at U5-spectroscopy beamline 09A2 in National Synchrotron Radiation Research Center (NSRRC) in Taiwan. To characterize the chemical and electronic structures, test samples with configurations ITO/NiO_{nc}/PbI_2 and ITO/NiO_{nc}/$MAPbI_3$ were prepared; ITO/PbI_2, ITO/$MAPbI_3$, and ITO/NiO_{nc} samples were fabricated as references for comparison. The dimensions of each sample for XPS, UPS, and measurement of NEXAFS were about 1.0 × 1.0 cm^2. Images from an O *K*-edge and Pb *N*-edge STXM were obtained at BL4U in UVSOR Synchrotron in Japan. In the STXM mapping measurements, a monochromatic X-ray beam was focused with a Fresnel zone plate to a 30 nm spot on the sample, which was raster-scanned with synchronized detection of transmitted X-rays to generate a sequence of images (stacks) over the range of

photon energies of interest; the intensities of the transmitted beam were measured at the image area detectors. All test films for STXM measurements were prepared on silicon nitride (SiN) membranes. Test samples with configurations SiN/NiO_{nc}, $SiN/NiO_{nc}/PbI_2$, and $SiN/NiO_{nc}/MAPbI_3$ were prepared for elemental mapping of STXM measurements.

Supporting Information

Supporting Information is available from the Wiley Online Library or from the author.

Acknowledgements

Ministry of Science and Technology (MOST 103-2112-M-213-007-MY3 and 103-2221-E-006-029-MY3) and National Synchrotron Radiation Research Center provided financial support of this work. P.C. appreciates financial support from the Top-Notch Project under the Headquarters of University Advancement at National Cheng Kung University, which is sponsored by Taiwan Ministry of Education. The authors also thank the financial support from the UVSOR-RIKEN collaboration program for STXM experiments.

Received: February 18, 2016
Revised: May 13, 2016
Published online:

[1] M. M. Lee, J. Teuscher, T. Miyasaka, T. N. Murakami, H. J. Snaith, *Science* **2012**, *338*, 643.
[2] A. Kojima, K. Teshima, Y. Shirai, T. Miyasaka, *J. Am. Chem. Soc.* **2009**, *131*, 6050.
[3] J.-H. Im, C.-R. Lee, J.-W. Lee, S.-W. Park, N.-G. Park, *Nanoscale* **2011**, *3*, 4088.
[4] D. B. Mitzi, S. Wang, C. A. Feild, C. A. Chess, A. M. Guloy, *Science* **1995**, *267*, 1473.
[5] Q. Chen, H. Zhou, Z. Hong, S. Luo, H.-S. Duan, H.-H. Wang, Y. Liu, G. Li, Y. Yang, *J. Am. Chem. Soc.* **2014**, *136*, 622.
[6] H.-S. Kim, C.-R. Lee, J.-H. Im, K.-B. Lee, T. Moehl, A. Marchioro, S.-J. Moon, R. Humphry-Baker, J.-H. Yum, J. E. Moser, M. Grätzel, N.-G. Park, *Nat. Sci. Rep.* **2012**, *2*, 591.
[7] S. D. Stranks, G. E. Eperon, G. Grancini, C. Menelaou, M. J. P. Alcocer, T. Leijtens, L. M. Herz, A. Petrozza, H. J. Snaith, *Science* **2013**, *342*, 341.
[8] G. Xing, N. Mathews, S. Sun, S. S. Lim, Y. M. Lam, M. Grätzel, S. Mhaisalkar, T. C. Sum, *Science* **2013**, *342*, 344.
[9] J. Fan, B. Jia, M. Gu, *Photon. Res.* **2014**, *2*, 111.
[10] H. Zhou, Q. Chen, G. Li, S. Luo, T.-B. Song, H.-S. Duan, Z. Hong, J. You, Y. Liu, Y. Yang, *Science* **2014**, *345*, 542.
[11] Research Cell Efficiency Records published by The National Center for Photovoltaics (NCPV) at NREL, http://www.nrel.gov/ncpv/images/efficiency_chart.jpg. *4*, **2016**.
[12] J. H. Kim, P.-W. Liang, S. T. Williams, N. Cho, C.-C. Chueh, M. S. Glaz, D. S. Ginger, A. K.-Y. Jen, *Adv. Mater.* **2015**, *27*, 695.
[13] K.-C. Wang, J.-Y. Jeng, P.-S. Shen, Y.-C. Chang, E. W.-G. Diau, C.-H. Tsai, T.-Y. Chao, H.-C. Hsu, P.-Y. Lin, P. Chen, T.-F. Guo, T.-C. Wen, *Sci. Rep.* **2014**, *4*, 4756.
[14] K.-C. Wang, P.-S. Shen, M.-H. Li, S. Chen, M.-W. Lin, P. Chen, T.-F. Guo, *ACS Appl. Mater. Interfaces* **2014**, *6*, 11851.
[15] M.-H. Li, P.-S. Shen, K.-C. Wang, T.-F. Guo, P. Chen, *J. Mater. Chem. A* **2015**, *3*, 9011.
[16] Z. Wu, S. Bai, J. Xiang, Z. Yuan, Y. Yang, W. Cui, X. Gao, Z. Liu, Y. Jin, B. Sun, *Nanoscale* **2014**, *6*, 10505.
[17] J.-Y. Jeng, K.-C. Chen, T.-Y. Chiang, P.-Y. Lin, T.-D. Tsai, Y.-C. Chang, T.-F. Guo, P. Chen, T.-C. Wen, Y.-J. Hsu, *Adv. Mater.* **2014**, *26*, 4107.
[18] J. H. Park, J. Seo, S. Park, S. S. Shin, Y. C. Kim, N. J. Jeon, H.-W. Shin, T. K. Ahn, J. H. Noh, S. C. Yoon, C. S. Hwang, S. I. Seok, *Adv. Mater.* **2015**, *27*, 4013.
[19] J. H. Heo, H. J. Han, D. Kim, T. K. Ahn, S. H. Im, *Energy Environ. Sci.* **2015**, *8*, 1602.
[20] H. Wang, P. Amsalem, G. Heimel, I. Salzmann, N. Koch, M. Oehzelt, *Adv. Mater.* **2014**, *26*, 925.
[21] D. Bi, L. Yang, G. Boschloo, A. Hagfeldt, E. M. J. Johansson, *J. Phys. Chem. Lett.* **2013**, *4*, 1532.
[22] V. Gonzalez-Pedro, E. J. Juarez-Perez, W.-S. Arsyad, E. M. Barea, F. Fabregat-Santiago, I. Mora-Sero, J. Bisquert, *Nano Lett.* **2014**, *14*, 888.
[23] M. K. Wang, C. Grätzel, S. M. Zakeeruddin, M. Grätzel, *Energy Environ. Sci.* **2012**, *5*, 9394.
[24] B. Cai, Y. Xing, Z. Yang, W.-H. Zhang, J. Qiu, *Energy Environ. Sci.* **2013**, *6*, 1480.
[25] W. Zhang, J. Smith, R. Hamilton, M. Heeney, J. Kirkpatrick, K. Song, S. E. Watkins, T. Anthopoulos, I. McCulloch, *J. Am. Chem. Soc.* **2009**, *131*, 10814.
[26] H.-Y. Hsu, C.-Y. Wang, A. Fathi, J.-W. Shiu, C.-C. Chung, P.-S. Shen, T.-F. Guo, P. Chen, Y.-P. Lee, E. W.-G. Diau, *Angew. Chem.* **2014**, *126*, 9493.
[27] C. D. Wagner, L. E. Davis, M. V. Zeller, J. A. Taylor, R. H. Raymond, L. H. Gale, *Surf. Interface Anal.* **1981**, *3*, 211.
[28] J. J. Yeh, I. Lindau, *Atom. Data Nucl. Data* **1985**, *32*, 1.
[29] R. Lindblad, D. Bi, B.-W. Park, J. Oscarsson, M. Gorgoi, H. Siegbahn, M. Odelius, E. M. J. Johansson, H. Rensmo, *J. Phys. Chem. Lett.* **2014**, *5*, 648.
[30] J. F. Moulder, W. F. Stickle, P. E. Sobol, K. D. Bomben, *Handbook of X-Ray Photoelectron Spectroscopy,* Physical Electronics Division, Eden Prairie, MN **1995**.
[31] A. Roy, D. D. Sarma, A. K. Sood, *Spectrochim. Acta, Part A: Mol. Spectrosc.* **1992**, *48*, 1779.
[32] D. V. Korolkov, G. P. Kostikova, Y. P. Kostikov, *Phys. C: Supercond.* **2002**, *383*, 117.
[33] S. Uhlenbrock, C. Scharfschwerdt, M. Neumann, G. Illing, H.-J. Freund, *J. Phys.: Condens. Matter* **1992**, *4*, 7973.
[34] A. R. González-Elipe, R. Alvarez, J. P. Holgado, J. P. Espinos, G. Munuera, J. M. Sanz, *Appl. Surf. Sci.* **1991**, *51*, 19.
[35] S. Oswald, W. Brückner, *Surf. Interface Anal.* **2004**, *36*, 17.
[36] E. L. Ratcliff, J. Meyer, K. Xerxes Steirer, A. Garcia, J. J. Berry, D. S. Ginley, D. C. Olson, A. Kahn, N. R. Armstrong, *Chem. Mater.* **2011**, *23*, 4988.
[37] C. C. Oey, A. B. Djurišić, C. Y. Kwong, C. H. Cheung, W. K. Chan, J. M. Nunzi, P. C. Chui, *Thin Solid Films* **2005**, *492*, 253.
[38] L. A. Grunes, R. D. Leapman, C. N. Wilker, R. Hoffmann, A. B. Kunz, *Phys. Rev. B* **1982**, *25*, 7157.
[39] I. Davoli, A. Marcelli, A. Bianconi, M. Tomellini, M. Fanfoni, *Phys. Rev. B* **1986**, *33*, 2979.
[40] S. Nakai, T. Mitsuishi, H. Sugawara, H. Maezawa, T. Matsukawa, S. Mitani, K. Yamasaki, T. Fujikawa, *Phys. Rev. B* **1987**, *36*, 9241.
[41] P. Kuiper, G. Kruizinga, J. Ghijsen, G. A. Sawatzky, H. Verweij, *Phys. Rev. Lett.* **1989**, *62*, 221.
[42] S. L. Dudarev, G. A. Botton, S. Y. Savrasov, C. J. Humphreys, A. P. Sutton, *Phys. Rev. B* **1998**, *57*, 1505.
[43] M. Finazzi, N. B. Brookes, *Phys. Rev. B* **1999**, *60*, 5354.
[44] S. L. Dudarev, M. R. Castell, G. A. Botton, S. Y. Savrasov, C. Muggelberg, G. A. D. Briggs, A. P. Sutton, D. T. Goddard, *Micron* **2000**, *31*, 363.

[45] F. M. F. de Groot, M. Grioni, J. C. Fuggle, J. Ghijsen, G. A. Sawatzky, H. Petersen, *Phys. Rev. B* **1989**, *40*, 5715.
[46] H. Kurata, E. Lefevre, C. Colliex, R. Brydson, *Phys. Rev. B* **1993**, *47*, 13763.
[47] Z. Y. Wu, S. Gota, F. Jollet, M. Pollak, M. Gautier-Soyer, C. R. Natoli, *Phys. Rev. B* **1997**, *55*, 2570.
[48] C. Colliex, T. Manoubi, C. Ortiz, *Phys. Rev. B* **1991**, *44*, 11402.
[49] W.-J. Yin, T. Shi, Y. Yan, *Appl. Phys. Lett.* **2014**, *104*, 063903.
[50] Y. Zhao, K. Zhu, *J. Phys. Chem. Lett.* **2013**, *4*, 2880.
[51] M. H. Kumar, N. Yantara, S. Dharani, M. Graetzel, S. Mhaisalkar, P. P. Boix, N. Mathews, *Chem. Commun.* **2013**, *49*, 11089.
[52] F. Brivio, A. B. Walker, A. Walsh, *APL Mater.* **2013**, *1*, 042111.
[53] Y. Wang, T. Gould, J. F. Dobson, H. Zhang, H. Yang, X. Yao, H. Zhao, *Phys. Chem. Chem. Phys.* **2014**, *16*, 1424.